Chromatic- and geometric-aberration-corrected TEM imaging at 80 kV and 20 kV

Felix Börrnert* and Ute Kaiser
Materialwissenschaftliche Elektronenmikroskopie, Universität Ulm, Albert-Einstein-Allee 11, 89081 Ulm, Germany

(Received 22 May 2018; published 30 August 2018)

The interest in light-element nanomaterials stimulated the development of atomic-resolution low-voltage transmission electron microscopy. While geometric-aberration correction made high-resolution imaging at around 80-kV electron acceleration voltage possible, imaging at substantially lower voltages requested the development of chromatic-aberration correction in addition. Recently, the SALVE instrument was introduced with the capability of atomic resolution imaging at electron acceleration voltages from 80 kV down to 20 kV. Here, we show on the example of imaging graphene that at these electron energies, the residual geometric aberrations reintroduce contrast oscillations and delocalization. Also, we show an atomically resolved image of a single vacancy in graphene with a pronounced Jahn-Teller distortion.

DOI: 10.1103/PhysRevA.98.023861

I. INTRODUCTION

Modern transmission electron microscopy has proven its capability in gaining unique knowledge about nanomaterials. Whereas the average atomic structure of bulk material is well known from diffraction techniques, the local structure of nanosized objects can only be retrieved by imaging techniques, that is, microscopy. The most widespread method that is able to deliver structural information down to the atomic level is transmission electron microscopy in its two variants of scanning (STEM) and conventional transmission electron microscopy (TEM).

When imaging a structure with high energy electrons, the electrons used for imaging have to interact with the object, thus introduce energy into it and often change the sample structure [1]. There are several different interaction mechanisms, with their respective interaction cross sections depending on the imaging electron energy (or electron accelerating voltage) [2]. The dominating sample damage mechanism is also strongly dependent on the respective sample properties. For instance, for the highly conductive carbon nanostructures, the so-called knock-on damage mechanism is dominating the sample destruction. Basically, this is elastic momentum transfer from the light electron to the much heavier atom core (not nucleus). If the energy transferred by this collision is large enough to overcome the binding energy of an atom inside its specific structure site, the atom is knocked out of its position. It is obvious that this process has a threshold energy for the incident electrons depending on the atom mass as well as on the bond strength towards its neighbors, i.e., the local sample structure. To stay with the example of carbon structures, the primary electron acceleration voltage needed to knock an atom out of a pristine sp^2 graphene lattice is around 80 kV when irradiating perpendicular to the graphene plane [3]. If the same carbon atom sits at a graphene edge or even in a single carbon chain, due to the different bond environment, the threshold electron acceleration voltage for knock-on damage can go down to about 20 kV [4].

On the other hand, to achieve an atomic level of image detail, the imaging electron acceleration voltage had to be raised to typically above 100 kV. Even with the latest geometric-aberration-corrector technology, true atomic resolution at lower energies is hard to achieve [5]. Here, the limiting factor is the energy distribution of the imaging electrons in combination with the chromatic aberration of the imaging system. In the era of geometric-aberration-corrected microscopes, monochromatization of the primary electrons became widespread to push this limit [6]. However, monochromatization reduces the available total signal substantially and does not act on electrons having lost energy due to interaction with the sample which are also participating in the imaging process and thus additionally reduces the signal-to-noise ratio in the image substantially.

Recently, we reported on the performance of a dedicated low-voltage transmission electron microscope that retains high resolution at electron acceleration voltages between 20 kV and 80 kV by means of chromatic-aberration correction in addition to geometric-aberration correction, the so-called SALVE (Sub-Ångström Low-Voltage Electron microscopy) instrument [7]. There, the energy distribution of the imaging electrons is not limiting the information transfer any more but the so-called Johnson-Nyquist noise [8]. In the present contribution, we report in detail about the imaging properties and conditions at the upper boundary of 80-kV and the lower boundary of 20-kV electron acceleration voltage. As a demonstration sample we use graphene.

II. EXPERIMENTAL

The TEM investigations were performed with the SALVE instrument consisting of a FEI Titan Themis[3] column fitted with a CEOS aberration corrector that corrects for first-order chromatic aberrations, axial geometric aberrations up to including the fifth order, and off-axial geometric aberrations

*felix.boerrnert@uni-ulm.de; Also at Leibniz-Institut für Festkörper- und Werkstoffforschung Dresden e. V., Helmholtzstraße 20, 01069 Dresden, Germany.

up to including the third order. The cameras used were a FEI CETA 16M fiber-coupled CMOS camera before and a Gatan UltraScan 1000XP fiber-coupled CCD camera behind an energy filter. In the latter case, the beam shutter used is in the energy filter, that is, behind the sample; then, the sample is irradiated continuously.

The sample is single-layer graphene grown by chemical vapor deposition and transferred onto standard Quantifoil TEM sample grids. While imaging, the samples were at room temperature.

In order to minimize the effect of the camera's modulation transfer function, but primarily to minimize the effect of Poisson noise by maximizing the camera's dynamic range, we chose a very high optical image magnification, that is, we largely oversample the images with camera pixels. This is necessary because of the high conversion rate of 14 counts/e^- (20 kV and 80 kV) for the CCD camera mounted behind the energy filter and its dynamic range limit of 2×10^4 counts/pixel in mean, i.e., a maximum of 1400 e^-/pixel in mean signal. The pixel size in the image is 7.1 pm (20 kV) and 7.8 pm (80 kV), therefore, assuming the theoretical Nyquist limit of two times the pixel size in combination with an assumed information limit of about 0.13 nm (20 kV) and 0.07 nm (80 kV), we oversample more than eight times (20 kV) or more than four times (80 kV). Thus, we increase the effective dynamic range to approximately 10^5 e^- mean signal per resolved image point. The camera's electron conversion rates for the different electron energies were calibrated with the help of a home-built Faraday cup at the sample position and the magnification calibration was done with the help of the known graphene periodicity.

All geometric aberrations up to the fifth order used in the calculations we measured with the Zemlin tableau method implemented in the CEOS corrector software with beam tilt angles of 45–55 mrad. The first-order chromatic aberrations were also measured with the help of the corrector software by varying the electron acceleration voltage and measure the effect on the image. The higher-order chromatic aberrations are measured and provided by CEOS GmbH, Heidelberg. For our calculations, we only consider the round aberrations since all unround aberrations are sufficiently small not to influence the results. The energy width of the primary electrons we measured using an imaging energy filter mounted to the microscope. We derived the illumination semiangle distribution by comparing the ratio of dose rates in combination with a previously measured value [9].

All images shown are unfiltered raw micrographs except the one in Fig. 3(a) where the filtering is stated explicitly and the original raw data is shown in Fig. 1(a). The Fourier transforms are cropped and contrast inverted for better visibility of the signals.

III. 80-kV IMAGING

Figure 1(a) shows a micrograph of graphene taken with a primary electron acceleration voltage of 80 kV. The micrograph is raw data without any filter applied. The imaging conditions were chosen to bear a positive contrast, i.e., the atoms appear bright on a dark background. These conditions are determined to offer the highest point resolution in

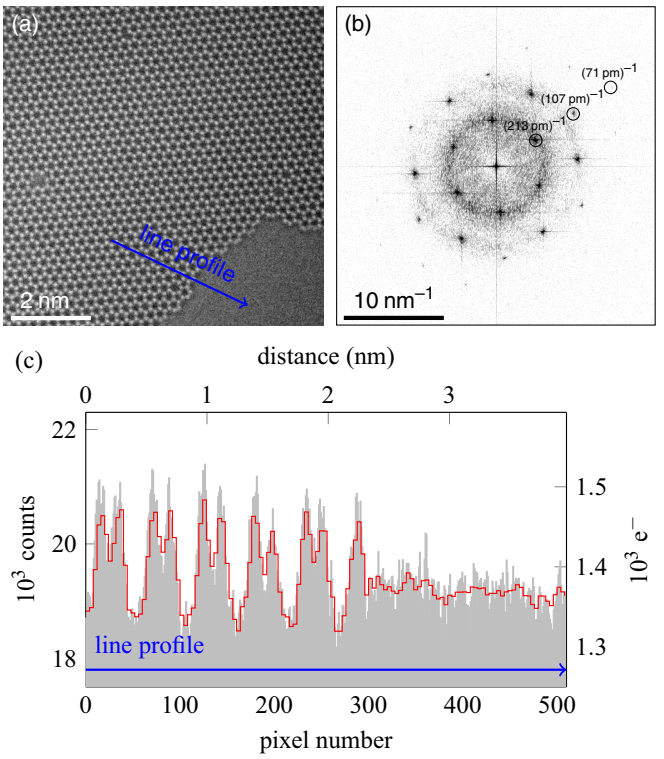

FIG. 1. Transmission electron micrograph of graphene taken with a primary electron acceleration voltage of 80 kV and positive contrast ("white-atom contrast"). (a) Section of the raw micrograph taken with a total dose of 2.3×10^7 e^-/nm^2 in 2-s exposure time, (b) Fourier transform of the micrograph featuring signals indicating a nonlinear information transfer up to at least 0.071 nm. The slight asymmetry in information transfer is due to sample drift. The background signal stems from amorphous residues in other regions of the full image (not shown). (c) The histogram in *gray* represents an intensity profile along the indicated line in (a); the line width is one pixel. Overlaid in *red* is an intensity profile along the same line in the same micrograph binned four times that shows a clear separation of the carbon atom positions.

combination with a minimum overall delocalization if one works with a fixed positive fifth-order spherical aberration (Lentzen conditions [10]). The corresponding defocus and third-order spherical aberration for the Lentzen conditions were calculated using the measured fifth-order spherical aberration.

In the lower right corner, a larger hole in the graphene sheet shows just vacuum. Besides two point defects, an edge and starting at the edge, an extended defect in the hexagonal lattice can be seen.

The Fourier transform or diffractogram shown in Fig. 1(b) bears signals indicating an information transfer up to 0.07 nm. The asymmetry in information transfer recognizable in the diffractogram is due to sample drift in combination with a comparably long exposure time as we can follow and quantify the sample drift over a series of successive images.

Along the indicated line in the micrograph we took an intensity profile plotted in Fig. 1(c). The right part going through vacuum indicates the Poisson noise level. All atom positions are clearly separated. The red line overlaid the raw

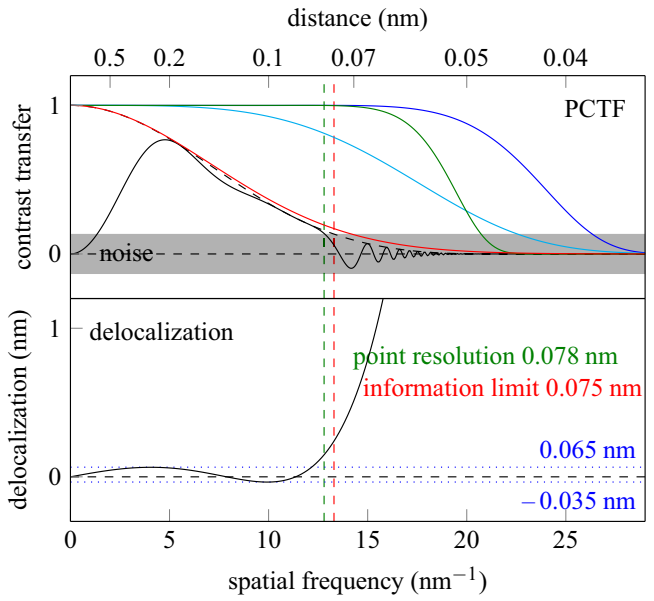

FIG. 2. Phase contrast transfer function and dampening envelope functions of the SALVE instrument at 80 kV with the measured fifth-order spherical aberration of 2.2 mm at Lentzen conditions plus a seventh-order spherical aberration of 62 mm. Black, phase contrast transfer; black dashed, total dampening, blue, chromatic dampening; cyan, residual focus spread dampening; green, illumination dampening; red, image spread dampening; and gray, noise. Below is the frequency-dependent delocalization function.

line scan signal is also a line scan along the same line but after binning the image four times. Both line scans have the same integration width of just one pixel. Of course, after binning, also the width of a single pixel is larger than in the unbinned image. The contrast of the carbon atoms in the image is about 10 % as can be read from the ordinate of Fig. 1(c).

In order to understand the TEM images better, we calculated the phase contrast transfer function (PCTF) and the frequency-dependent delocalization of the SALVE instrument at 80-kV electron acceleration voltage using the measured imaging condition parameters.

All calculations are in the frame of linear contrast transfer. An exact description of the contrast transfer would be a complex integration of the object spectrum including the transmission cross coefficient [11]. Unfortunately, there is no easily comprehensible way to describe the dampening action for arbitrary objects in the frame of the transmission cross coefficient since it is object dependent. Nevertheless, the mathematical description of the dampening mechanism in the linear framework is a border case that securely gives the minimum information transfer.

Both, the PCTF and the frequency-dependent delocalization are plotted in Fig. 2. In the upper panel, apart from the PCTF drawn in black, we also show the four most prominent dampening envelope functions: the illumination dampening in green, the chromatic dampening in blue, the residual focus spread dampening in cyan, and the image spread dampening in red. Obviously, the latter is the dominating contrast dampening mechanism. For all dampening functions, the worst case scenario has been applied and several necessary refinements to the traditional descriptions have been made; see the Appendix. The gray shaded area represents the noise level that is conventionally assumed as e^{-2} of the total contrast. This convention is still meaningful today because the noise is dominated by the Poisson noise of the imaging electrons themselves, and thus, the noise level is mainly dependent on the total electron dose in the image regardless of the detector. The information limit is the point where the total dampening envelope function enters the noise level, and similarly, the point resolution is given by the lowest spatial frequency where the PCTF enters the noise level.

Near the Gaussian focus (defocus equals zero) the absolute value of the defocus is unknown in geometrical-aberration-corrected microscopes since there are no Thon rings, i.e., oscillations in the PCTF above noise level. In the imaging process, we installed the right defocus for Lentzen conditions by maximizing the image contrast with the atoms appearing bright and additionally let no Thon rings occur in the Fourier transform of the image, since all neighboring defocus values with white-atom contrast for graphene must show two Thon rings below the lowest graphene reflex frequency as might become clear when looking at Figs. 8 and 9 further down. Amorphous residues on top of the graphene for the potential Thon rings are always in the full field of view.

The parameters for the illumination dampening are the measured geometric aberrations and an illumination semiangle distribution of 0.16 mrad. A focus spread of maximal 0.5 nm is estimated from the measured chromatic aberration and electron energy distribution and additionally is well in the upper limit (<1 nm) determined previously [7]. The highest-order signals in the diffractogram of the graphene image are only visible due to nonlinear information transfer because they are beyond the information limit. Nevertheless, in contrast to the other dampening mechanisms, image spread would destroy any nonlinear contrast transfer as well [8,12]. Therefore, we can say that the highest nonlinearly transferred signals are inside the image spread envelope and thus find a maximum value for the image spread of 22.5 pm at 80 kV.

In the lower panel of Fig. 2, the corresponding frequency-dependent delocalization is shown. The absolute delocalization value stays below the information limit value up to the point resolution spatial frequency of 12.8 nm^{-1} and thus does not play a role.

In order to reveal defects in the lattice, a handy way is to filter the perfect lattice from the original micrograph by means of a mask in the Fourier space. Figure 3(a) a filtered version of the micrograph in Fig. 1(a). The arrow in there points to a defect position that we cut from the original micrograph and show in Fig. 3(b). It is clearly a single vacancy. A pronounced asymmetry of the defect is clearly recognizable. This kind of distortion is due to the electronic properties of a single vacancy in graphene and is called Jahn-Teller distortion [13], which to the best of our knowledge has not been directly imaged at true atomic resolution before.

IV. 20-kV IMAGING

Figure 4(a) shows a micrograph of graphene with some amorphous carbon residues taken at 20-kV electron acceleration voltage. Again, the imaging conditions were chosen to bear a positive contrast, as in the 80-kV case.

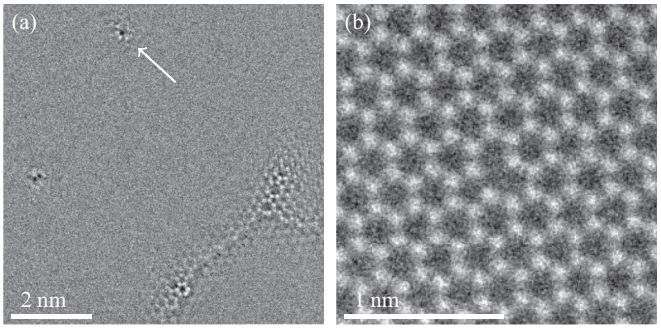

FIG. 3. Defect analysis of the micrograph in Fig. 1. (a) Fourier filtered version of the micrograph, the basic graphene lattice removed. Only defects and the edge show structure. (b) Enlarged detail from the original micrograph at the position indicated by the arrow in (a) showing a single vacancy featuring a pronounced Jahn-Teller distortion.

The second-order signals in the diffractogram shown in Fig. 4(b) suggest an information transfer of at least up to 0.123 nm. That we indeed have an information transfer of at least 0.14 nm can be deduced from the intensity profile in Fig. 4(c) along the indicated line in Fig. 4(a). Here, the

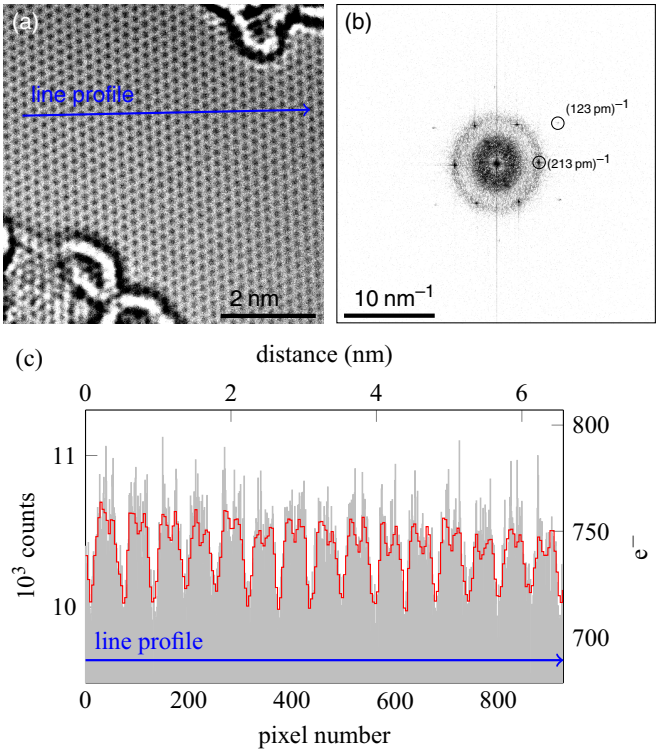

FIG. 4. Transmission electron micrograph of graphene taken with a primary electron energy of 20 keV and positive contrast ("white-atom contrast"). (a) The raw micrograph taken with a total dose of 1.5×10^7 e$^-$/nm^2 in 2-s exposure time. (b) Fourier transform of the micrograph featuring a complete set of second-order spots indicating an isotropic nonlinear information transfer up to at least 0.123 nm. (c) The histogram in *gray* represents an intensity profile along the indicated line in (a); the line width is one pixel. Overlaid in *red* is an intensity profile along the same line in the same micrograph binned four times that shows a clear separation of the carbon atom positions.

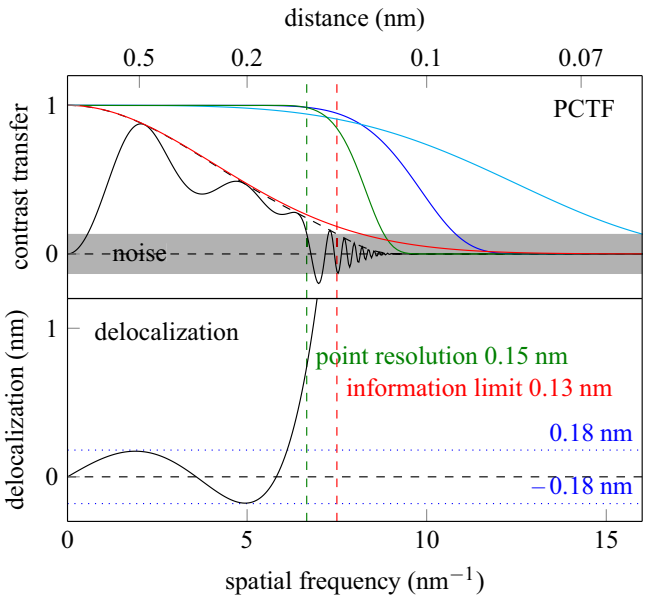

FIG. 5. Phase contrast transfer function and dampening envelope functions of the SALVE instrument at 20 kV with the measured fifth-order spherical aberration of 6.7 mm at Lentzen conditions plus a seventh-order spherical aberration of 62 mm. Black, phase contrast transfer; black dashed, total dampening; blue, chromatic dampening; cyan, residual focus spread dampening; green, illumination dampening; red, image spread dampening; and gray, noise. Below is the frequency-dependent delocalization function.

histogram shows the raw signal with considerable shot noise due to the statistics in each pixel since we got a mean overall signal of about 40 electrons on a 700-electron background. Note that we did not integrate over several pixels perpendicular to the scan line. By binning four times, we enhance the signal by a factor of 16 without losing image resolution because we largely oversampled the image in the beginning with a factor of more than eight. The binned signal (normalized to the original intensity) represented by the red line shows clearly resolved carbon atom positions with a distance of 0.14 nm. The contrast obtained from the graphene lattice is about 7 % [cf. the intensity profile in Fig. 4(c)].

Figure 5 shows the equivalent information for 20-kV electron acceleration voltage as Fig. 2 for 80 kV with the same encoding scheme. Here, the illumination semiangle distribution was determined to be 0.32 mrad. Also, from the highest-frequency signals transferred, we confirm the image spread value predicted before [14]: The maximum value for the image spread is 39 pm at 20 kV.

From the PCTF as shown in Fig. 5 we read an information limit of 0.13 nm at 20-kV electron acceleration voltage. In Fourier space this means a 64-mrad open phase plate and an information limit of about 15.5 times the wavelength of the imaging electrons. Nevertheless, the calculated point resolution is still at about 0.15 nm due to the residual fifth-order spherical aberration of 6.7 mm. Thus, the information limit is beyond the point resolution again like in the classical uncorrected TEM case. For the image presented in Fig. 4 we therefore derive that most probably the second-order signals in the Fourier transform are pure nonlinear information transfer.

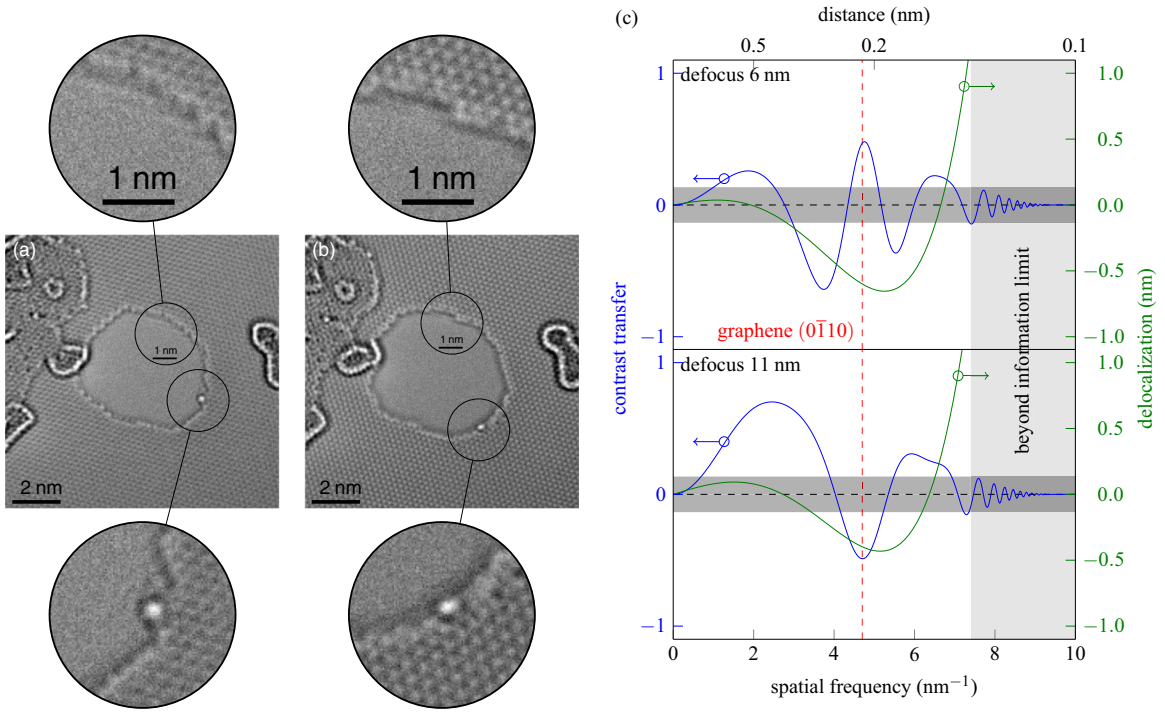

FIG. 6. Transmission electron micrographs of a hole in graphene with a heavier atom attached taken with a primary electron energy of 20 keV. The images shown are raw micrographs taken with a dose of 8.5×10^6 e$^-$/nm^2 in 4-s exposure time. A different defocus chosen for each image results in (a) positive and (b) negative contrast of the carbon lattice. Note that the contrast of the heavier atom remains positive. The irradiation time between both images was 40 s with a dose rate of 2.1×10^6 e$^-$/(nm^2 s), i.e., a total dose of 8.5×10^7 e$^-$/nm^2. (c) Phase contrast transfer functions (blue) and frequency-dependent delocalization (green) for the micrographs. The upper graph is for a defocus of 6 nm and the lower for 11 nm. The dashed red line indicates the lowest-frequency graphene signal.

Also, the separation of the carbon atom positions is definitely beyond the point resolution.

In the lower panel of Fig. 5, the corresponding frequency-dependent delocalization is shown. The absolute delocalization value stays in the boundary of 0.18 nm within the majority of the main transfer band, but at the high frequency side it grows considerably. Already a delocalization value of 0.18 nm is distinctly larger than the point resolution of 0.15 nm.

Figures 6(a) and 6(b) show two micrographs of the same hole in graphene. An interesting feature is the contrast reversal between positive contrast for the graphene lattice in Fig. 6(a) and negative contrast in Fig. 6(b) due to a slight drift along the optical axis. Note that the heavy atom attached to the edge of the hole does not reverse its contrast; it remains bright. This is due to the breakdown of the weak phase object approximation for not-so-light elements at low electron energies.

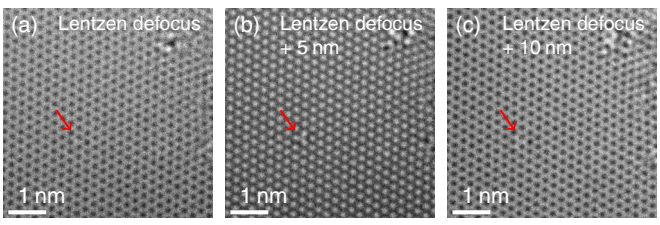

FIG. 7. Series of successive transmission electron micrographs of a single vacancy in graphene taken with 20-kV electron acceleration voltage. (a) Defocus at Lentzen condition value (positive contrast), (b) 5 nm more defocus (negative contrast), and (c) 10 nm more defocus (positive contrast again).

The edges in Fig. 6(a) show clear signs of delocalization while delocalization is smaller in Fig. 6(b); see the fringelike contrast reaching into the vacuum region in the upper magnification circles. As mentioned earlier, the delocalization at the first-order graphene signal of 4.7 nm^{-1} within Lentzen conditions is about 0.18 nm. Therefore, we calculated the PCTF and frequency-dependent delocalization of the neighboring contrast transfer pass bands, see Fig. 6(c), and got a decent match of the delocalization width for the defoci of 6 nm (0.6-nm delocalization, positive contrast) and 11 nm (0.4-nm delocalization, negative contrast), respectively.

The time under irradiation elapsed between the images in Fig. 6 is 36 s (plus 4-s initial exposure time), but more important, the electron dose in between was about 8.5×10^7 e$^-$/nm^2. Apparently, the hole grew between the imaging times with its diameter increasing approximately 0.5 nm in average in each direction. This corresponds to approximately one unit cell per edge per 10^8 e$^-$/nm^2.

A demonstration of a good resolution at 20-kV electron acceleration voltage is the image of a single vacancy in graphene in Fig. 7(b). The missing atom is clearly resolved. Surprisingly, the single vacancy is only visible at a certain defined negative contrast condition ("black atom contrast"). The higher-order aberrations are well controlled and we did not find any defocus with positive contrast that showed this single

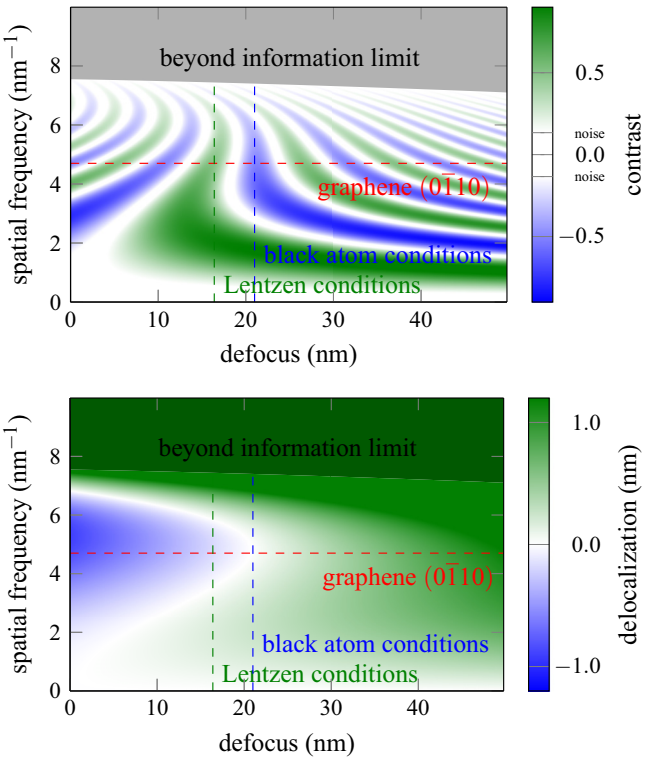

FIG. 8. Phase contrast transfer function (top) and delocalization (bottom) in dependence of the defocus for 20-kV electron acceleration voltage. Indicated in red is the signal frequency of the graphene lattice, in green the defocus of the Lentzen conditions ("white atom contrast") for the specific measured fifth-order spherical aberration of 6.7 mm, and in blue the respective neighboring black atom contrast defocus. The gray shaded area shows the frequencies beyond the information limit calculated as in Ref. [9].

vacancy in graphene as would be expected for the installed Lentzen conditions (apart from the defocus).

In order to understand this phenomenon, we investigate the changes in the PCTF (top) and the frequency-dependent delocalization (bottom) with varying defocus, as shown in Fig. 8. For the PCTF, the green color represents positive contrast transfer and blue negative contrast transfer. The dashed green line indicates the exact Lentzen conditions and the profile along it is the PCTF (and frequency-dependent delocalization) shown in Fig. 5. Additionally, the lowest spatial frequency of graphene is indicated in red.

A first observation is that at Lentzen defocus, the delocalization for graphene's specific spatial frequency of 4.7 nm^{-1} is about 0.18 nm (see also Fig. 5). Since the atom spacing is 0.14 nm, a "phantom" atom might be reconstructed in the single vacancy by delocalization. In the neighboring negative transfer band indicated by the dashed blue line, the delocalization for the graphene frequency is zero. This explains why we see the single vacancy only at black atom conditions.

At the end of this section, we want to shortly discuss the effect of lowering the electron energy on the beam brightness. Since the reduced brightness is an intrinsic property of the electron source and thus constant, the brightness scales with the relativistically modified acceleration voltage. In rough approximation, the total current that the electron source provides can be put through the sample independent of the acceleration voltage if the condenser aperture system is variable enough. Only, one has to bear in mind that the illumination semiangle distribution is enlarged accordingly due to the relation for all angles $\theta = \lambda q$, with λ being the wavelength and q the spatial frequency. At 20-kV electron acceleration voltage and 6.7-mm fifth-order spherical aberration, there is already a significant contribution of the illumination dampening to the total contrast dampening due to the large illumination semiangle distribution. In imaging modes where the spatial coherence matters much, e.g., holography, the impact might be more serious.

V. DEPTH OF FOCUS

When looking at the change of the PCTF with the defocus in Fig. 8, a striking feature is the reversed-S shape of the Lentzen pass band. Here, it becomes intuitively clear where the local minima in the PCTF originate from. Also, it becomes obvious that any tiny deviation from the exact defocus of the Lentzen conditions results into transfer gaps or even contrast reversal bands in the original frequency pass band. From the plot, it can be read that the defocus variation where the full pass band remains positive is about 1 nm at maximum; even in this small variation region, there are substantial drops in the contrast transfer magnitude. Depth of focus we call here a defocus range where a certain single contrast transfer band has contrast transfer for all its spatial frequencies without substantial cuts in the magnitude.

The mentioned reversed-S shape of the transfer bands originates from the finite fifth-order spherical aberration and its compensation by the third-order spherical aberration. If one minimizes the fifth-order spherical aberration, this shape straightens considerably, as shown in Fig. 9. A common argument for leaving a certain residual fifth-order spherical aberration is that the integrated contrast over the pass band is higher, especially at lower frequencies. This argument still holds true but is in this case out-weighted by the impractically high demands for the defocus precision and thus the depth of focus. Moreover, if we look at the frequency-dependent delocalization in the lower panel of Fig. 9, in Lentzen conditions, the delocalization stays below 0.1 nm which is less than the information limit of 0.13 nm.

In both cases, if we just consider the single graphene signal frequency at 4.7 nm^{-1}, the focus width of any transfer band is about 5.3 nm from contrast reversal to contrast reversal. Of course, this cannot be counted as depth of focus, even not for this single frequency. In the single graphene frequency case, we would estimate a depth of focus of 3 nm at maximum because one needs a certain minimum contrast transfer to image any structure, but around the contrast reversal point, the contrast transfer is zero. Nevertheless, since considering only the transfer of a single frequency for microscopic imaging has no meaning at all, we have to consider the complete pass band up to the point resolution. Here, the focus distance between the neighboring contrast reversals at point resolution frequency is 2.1 nm, making the real depth of focus approximately 1 nm, but only in the case with the assumed small fifth-order spherical aberration.

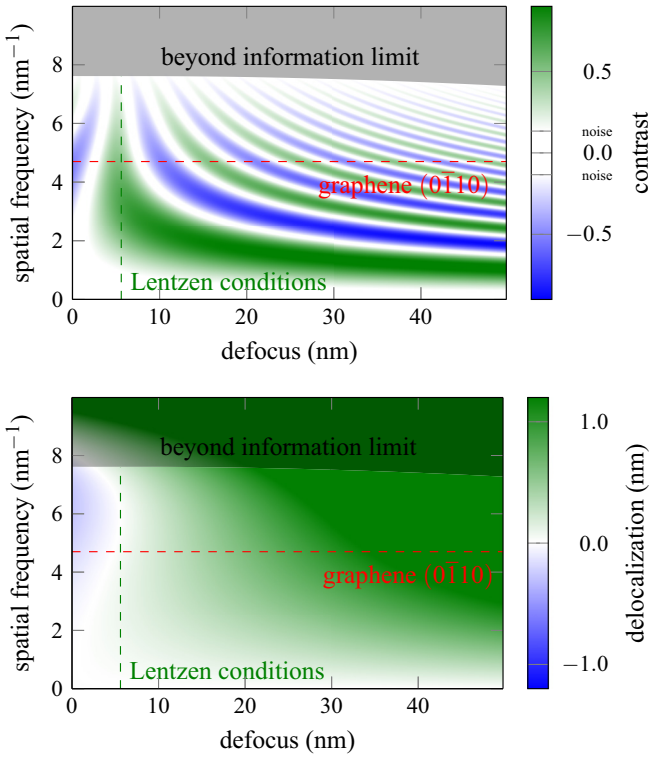

FIG. 9. Same as Fig. 8 but with an assumed fifth-order spherical aberration of 0.5 mm and an accordingly changed third-order spherical aberration for adapted Lentzen conditions.

Anyway, the experienced microscopist may already have observed in Fig. 4 that the amorphous residuals on the graphene appear largely out of focus. To test the depth of focus, we made a simple experiment: We tilted a single-layer graphene sample to 30° as well as −30° and imaged it; see Fig. 10. In other words, we use an ultimately thin sample and put it into many different defoci in the same image. Because we had to ensure a certain field of view, we used a comparably low magnification while still resolving the graphene lattice. Because of this, the image contrast is quite low but one can distinctly recognize the regions of zero contrast.

The dashed lines in Fig. 10 indicate lines of visually highest graphene lattice contrast parallel to the tilt axis. The distance of these lines is about 9 nm. With the help of basic trigonometry, we derive a focus distance between two contrast maxima of 5.2 nm. This result fits well the value of 5.3 nm read from the calculations. It definitely shows that the focus depth in TEM images taken with 20-kV electron acceleration voltage is in the order of a few nanometers.

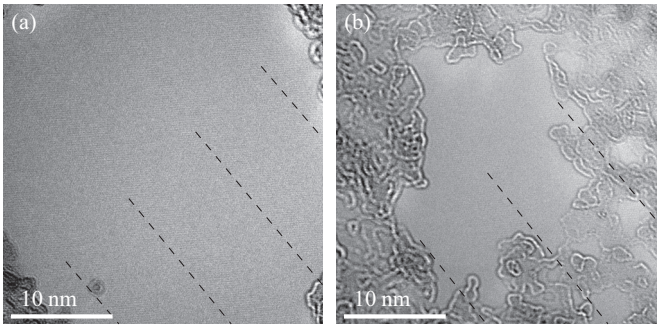

FIG. 10. Transmission electron micrograph of graphene taken with 20-kV electron acceleration voltage and with a sample tilt angle of (a) 30° and (b) −30°. The lines are indicating regions of largest lattice contrast; in between, the lattice contrast goes to zero.

VI. DISCUSSION

Let us now discuss our results with respect to nowadays commercially available high-end instrumentation and other dedicated low-voltage TEM approaches.

As already mentioned in the introduction, the SALVE instrument's information transfer limit is not set by the focus spread dampening any more, but is dominated by Johnson-Nyquist noise resulting in image spread [8]; however, this limiting factor can also be advantageous in one respect, as it acts on nonlinear information transfer the same way as on linear transfer. Thus, most information we see is inside the boundaries of the information limit. For non-chromatic-aberration-corrected imaging—especially at low acceleration voltages—the high spatial frequency information is in many cases only nonlinear information transfer [5].

As a result of the just mentioned nonlinear information transfer, the resolving power of the latest high-end microscopes often is overestimated. As an example, the nonmonochromated FEI Titan has an information limit of 0.19 nm at 80-kV electron acceleration voltage [5], but very often, an information transfer of 0.12 nm was reported because of the nonlinear second-order signals of graphene in diffractograms. For the SALVE instrument, we now demonstrated a linear information transfer up to about 0.13 nm at 20-kV electron acceleration voltage.

A widespread way to enhance the resolving power of geometric-aberration-corrected microscopes is the monochromatization of the primary electrons [6]. Theoretically, by this means one can reduce the focus spread in a similar magnitude like with chromatic-aberration correction if one cuts the energy distribution width sufficiently. Practically, one loses most of the available electrons for imaging and thus usable signal. Additionally, inelastically scattered electrons are not only lost for the imaging process but also increase the noise level in the images. With chromatic-aberration correction, the whole total current of the electron source can be used for imaging without compromising the information transfer and inelastically scattered electrons still contribute to the image.

Another means used to increase the information transfer additionally to the monochromatization approach is the use of extremely narrow objective lens pole piece gaps [15]. While this effectively reduces geometric and chromatic aberrations by a factor of about one-half, the space for handling the actual sample is minimized. With such pole pieces one needs special extra-flat sample holders, the sample tilting range is severely limited, and *in situ* experiments are very much harder to implement. The SALVE instrument has a standard pole piece gap of 5.4 mm where the whole range of commercially available *in situ* sample holders fits into.

VII. SUMMARY

We evaluated the imaging properties in chromatic- and geometric-aberration-corrected TEM at electron acceleration voltages of 80 kV and 20 kV on the example of graphene images using the SALVE instrument. For the 80-kV case, we determined an image point resolution of 0.078 nm and an information limit of 0.075 nm. At 20 kV, apart from the very decent resolving power of 0.15-nm point resolution and at least 0.13-nm information transfer, we identified substantial delocalization stemming from the finite fifth-order spherical aberration. A depth of focus in the nanometer range was found. Additionally, we showed a clear atomic-level image of a single vacancy in graphene with a pronounced Jahn-Teller distortion.

Finally, we conclude that the approach using chromatic-aberration correction in addition to geometric-aberration correction in low-voltage TEM is greatly beneficial for *in situ* imaging with atomic resolution.

ACKNOWLEDGMENTS

We thank Martin Linck and Heiko Müller (CEOS GmbH, Heidelberg) as well as Harald Rose (Universität Ulm) for valuable discussions and Tibor Lehnert (Universität Ulm) for the sample preparation. We acknowledge funding from the Deutsche Forschungsgemeinschaft (DFG) and the Ministerium für Wissenschaft, Forschung und Kunst Baden-Württemberg, Germany, in the frame of the SALVE project (Grant No. KA1295/12-2).

APPENDIX: CONTRAST DAMPENING FUNCTIONS

For the dampening envelope functions we had to introduce some refinements to the traditionally applied ones since in the case of aberration correction, some approximations therein are not valid any more. In the following, we only consider round aberrations, assuming all relevant unround aberrations to be corrected to zero which is valid for a well-aligned instrument.

When dealing with the illumination dampening function, one starts with the general expression,

$$E_{\mathrm{illu}}(q) = e^{-\frac{1}{2}\left(\frac{2\pi}{\lambda}\,\sigma_\alpha\,\nabla\chi\right)^2},$$
$$\nabla\chi = C_1(\lambda q) + C_3(\lambda q)^3 + C_5(\lambda q)^5 + C_7(\lambda q)^7 + \ldots, \tag{A1}$$

with λ the electron wavelength, σ_α the illumination semi-angle distribution, χ the aberration function, C_i the geometric-aberration coefficients (C_1 being the defocus), and (λq) the scattering angle. Here, we are taking into account only the round geometric aberrations C_i. In the case of microscopes without geometric-aberration correction, the first term of the series dominated the expression and thus, the series was ended just there; unfortunately, for geometric-aberration-corrected microscopes, this would give virtually no dampening at all, which is not true by far:

$$E_{\mathrm{illu}}(q) \not\approx e^{-2\pi^2\,\sigma_\alpha^2\,C_1^2\,q^2}. \tag{A2}$$

In some places, one finds the third-order spherical aberration considered in addition [16,17]; for our case, a more realistic approximation is if we consider the first four terms of the round geometric-aberration series as demonstrated below:

$$E_{\mathrm{illu}}(q) \approx e^{-\frac{2\pi^2}{\lambda^2}\,\sigma_\alpha^2\,\left(C_1(\lambda q)+C_3(\lambda q)^3+C_5(\lambda q)^5+C_7(\lambda q)^7\right)^2}. \tag{A3}$$

In order to get a realistic value for the illumination semiangle distribution, we measured it once by a defocus series method for this microscope and electron acceleration voltage [9]. Considering that the reduced brightness B_r is an intrinsic property of the electron source, one derives

$$B_r = \frac{j}{\Delta\Omega\,U^*}, \quad \Delta\Omega \approx \pi\sigma_\alpha^2 \quad \Rightarrow \quad \sigma_\alpha^2 \approx \frac{j}{\pi\;B_r\;U^*}, \tag{A4}$$

with the current density j, the solid angle $\Delta\Omega$, and the relativistically modified electron acceleration voltage U^*. From here, one obtains the per-image value for σ_α *via* the current density ratio,

$$\frac{\sigma_\alpha^2(1)}{\sigma_\alpha^2(2)} = \frac{j(1)}{j(2)}. \tag{A5}$$

The current density can be read directly from any phase-contrast image with a calibrated conversion rate and known acquisition time.

Figure 11 demonstrates the effect of taking higher-order terms of the aberration function series into account in the illumination dampening function. It is obvious that neglecting at least the third- and fifth-order spherical aberration C_3 and C_5 leads to substantially wrong results. In turn, the seventh-order spherical aberration C_7 does not change the result noticeably, which is good since it is inherently difficult to measure, at least without chromatic-aberration correction. The attentive observer might recognize that incorporating the fifth-order spherical aberration into the dampening envelope is extending it considerably. This is due to a counterbalancing mechanism already used for the Lichte defocus [16]. In general, the illumination dampening treatment up to the fifth-order spherical aberration is necessary in any third-order

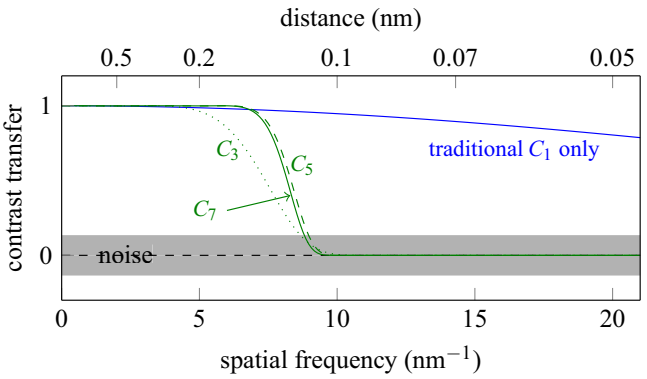

FIG. 11. Illumination dampening functions for 20-kV electron acceleration voltage. The traditional expression (A2) with only the defocus taken into account is plotted in blue. Functions after Eq. (A3) with successively added higher-order terms are drawn in green with a label indicating the respective highest-order aberration taken into account. The parameters used for this calculation are $\sigma_\alpha = 0.32$ mrad, $C_1 = 16.4$ nm, $C_3 = 23.7$ µm, $C_5 = 6.7$ mm, and $C_7 = 62$ mm as installed and measured at the SALVE instrument as Lentzen conditions for a finite C_5.

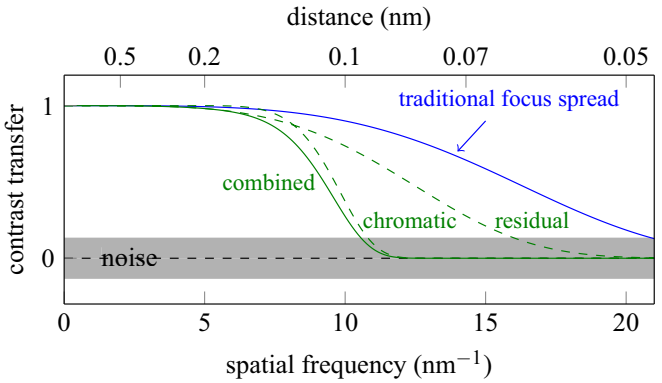

FIG. 12. Focus spread dampening functions for 20-kV electron acceleration voltage. Drawn in blue is the traditional focus spread function after Eqs. (A7) and (A8). Both the dashed green lines represent the residual focus spread dampening and the correct chromatic dampening, respectively. The combined effect of these latter two functions is drawn in solid green. The parameters used for this calculation are $C_{c,\mathrm{OL}} = 1.45$ mm, $(\frac{\Delta I}{I})_{\mathrm{OL}} = 10^{-7}$, $C_{c,\mathrm{MP}} = 1.45$ mm, $(\frac{\Delta I}{I})_{\mathrm{MP}} = 10^{-8}$, $C_{1c}^{(1)} = -10$ µm, $C_{3c}^{(1)} = 11$ mm, $(\frac{\Delta U}{U}) = 10^{-6}$, $\Delta E_e = 0.34$ eV (equivalent to 0.8 eV FWHM).

spherical-aberration-corrected microscope to be correct. In these, at higher electron energies and normal imaging modes, the focus spread dampening is much dominant over the illumination dampening. Nevertheless, for some special imaging modes like incoherent or hollow-cone illumination or imaging with highly monochromated electrons it might become important.

When it comes to focus spread dampening, textbooks give a general origin of the function and following its final expression as [17]

$$E_{\mathrm{fs}}(q) = e^{-\frac{1}{2}\left(\frac{2\pi}{\lambda}\,\sigma_{\mathrm{fs}}\,\frac{\partial\chi}{\partial C_1}\right)^2}, \quad \frac{\partial\chi}{\partial C_1} = \tfrac{1}{2}(\lambda q)^2, \tag{A6}$$

$$E_{\mathrm{fs}}(q) = e^{-\frac{\pi^2}{2\lambda^2}\,\sigma_{\mathrm{fs}}^2\,(\lambda q)^4}, \tag{A7}$$

with the focus spread,

$$\sigma_{\mathrm{fs}} = C_c\sqrt{\left(\tfrac{\Delta U}{U}\right)^2 + \left(\tfrac{\Delta E_e}{eU}\right)^2 + \left(2\tfrac{\Delta I}{I}\right)^2}, \tag{A8}$$

with the chromatic-aberration coefficient C_c, the high tension stability $(\frac{\Delta U}{U})$, the electron emission energy distribution ΔE_e, and the objective lens current stability $(\frac{\Delta I}{I})$.

The derivation in Eq. (A6) inherently assumes that we face only a focus variation as we differentiate the aberration series with respect to the defocus. In the first place this is correct since we call it focus spread and thus are only looking at the focus variation. Thinking on, the assumption that the underlying basic mechanisms, i.e., the variation of the primary electron energy and, completely independent, the variation of the focusing strength of the objective lens, is not valid, at least for the former one.

In the case of chromatic-aberration-corrected imaging, we have to split the two basic mechanisms into two separate functions for the chromatic dampening and the residual focus spread dampening,

$$E_{\text{`fs'}}(q) = E_{\mathrm{cc}}(q)E_{\mathrm{fs,\,residual}}(q). \tag{A9}$$

Starting at the lens instabilities, the chromatic-aberration correction does not at all affect the effect of these on the focus spread since the corrector does not know anything about the actual fluctuation of the lens current. Therefore, the traditional expression (A7) and its derivation still holds true, in fact, with the original chromatic-aberration coefficient of the single element in question. Formerly, we had only to consider the objective lens current fluctuations because it dominated the chromatic-aberration effects. Now, we introduced two other elements with the same absolute chromatic aberration for the compensation of the objective lens aberration and have to add their instability effect. Fortunately, we can combine their effect into one because of their action on orthogonal line foci. Consequently,

$$\sigma_{\mathrm{fs,\,residual}} = \sqrt{\sum_i C_{c,i}^2\left(a\tfrac{\Delta I}{I}\right)_i^2}, \tag{A10}$$

with i indicating the single optical elements and $a_i = 2$ for round lenses and $a_i = 1$ for multipoles. Also, each element has its own (uncompensated) chromatic-aberration coefficient.

For the electron-energy-dependent part, the chromatic-aberration correction changes the game substantially. Here, we have to consider an energy-dependent aberration function series,

$$\chi\left(\tfrac{\Delta E}{E_0}\right) = \sum_{i=0}^{\infty}\chi^{(i)}\left(\tfrac{\Delta E}{E_0}\right)^i, \tag{A11}$$

where $\chi^{(0)}$ is the known (energy-independent) geometric-aberration function. Since our energy deviation is small, we can break the series after the second term, thus,

$$\begin{aligned} E_{\mathrm{cc}}(q) &= e^{-\frac{1}{2}\left(\frac{2\pi}{\lambda}\,\sigma_E\,\frac{\partial\chi}{\partial\frac{\Delta E}{E_0}}\right)^2}, \\ \frac{\partial\chi}{\partial\frac{\Delta E}{E_0}} &\approx \frac{\partial\chi^{(1)}}{\partial\frac{\Delta E}{E_0}} \\ &= \tfrac{1}{2}C_{1c}^{(1)}(\lambda q)^2 + \tfrac{1}{4}C_{3c}^{(1)}(\lambda q)^4 + \ldots, \\ \sigma_E &= \sqrt{\left(\tfrac{\Delta U}{U}\right)^2 + \left(\tfrac{\Delta E_e}{eU}\right)^2}. \end{aligned} \tag{A12}$$

The series has "only" an approximate sign because the series is itself only the first term of another power series of $(\frac{\Delta E}{E_0})^n$. In turn, this ratio is fairly small, thus we can safely neglect higher orders in this case if we just consider the fully elastic part of the imaging, i.e., the energy distribution of the primary electrons. For energy-filtered TEM with large energy windows or the imaging with substantial contribution from plasmon-loss electrons, one might have to consider the higher-order terms of the secondary series as well. For our case, it is sufficient to break the remaining series after the third-order chromato-spherical aberration $C_{3c}^{(1)}$ [18].

As a consequence, the chromatic spread is no pure focus spread any more. If we nevertheless wanted to squeeze the updated description into the structure of Eq. (A7), we could write a virtual focus spread,

$$\sigma_{\mathrm{fs,\,chrom.}}(\mathrm{virtual}) \approx \left(C_{1c} + \tfrac{1}{2}C_{3c}(\lambda q)^2\right)\sqrt{\left(\tfrac{\Delta U}{U}\right)^2 + \left(\tfrac{\Delta E_e}{eU}\right)^2}. \tag{A13}$$

At this point, it also becomes apparent that with a variable chromatic-aberration coefficient C_{1c}, we do not want to compensate it to zero but to a "chromatic-Scherzer-like" condition.

In Fig. 12, we compare results from the traditional focus spread description to the combination of the correct residual focus spread and chromatic spread dampening. Also here, the necessity of revisiting the contrast dampening description is obvious. This refinement in turn is only necessary for chromatic-aberration-corrected imaging; even for imaging with highly monochromated imaging electrons the original approximation is sufficient.

Just for completeness, the image spread dampening we describe as

$$E_{\mathrm{is}}(q) = e^{-\frac{1}{2}\left(\frac{2\pi}{\lambda}\,\sigma_{\mathrm{is}}\,(\lambda q)\right)^2}, \tag{A14}$$

with the image spread σ_{is}.

[1] D. Gabor, Rev. Mod. Phys. **28**, 260 (1956).
[2] F. Banhart, Rep. Prog. Phys. **62**, 1181 (1999).
[3] J. C. Meyer, F. Eder, S. Kurasch, V. Skakalova, J. Kotakoski, H. J. Park, S. Roth, A. Chuvilin, S. Eyhusen, G. Benner, A. V. Krasheninnikov, and U. Kaiser, Phys. Rev. Lett. **108**, 196102 (2012).
[4] D. C. Bell, C. J. Russo, and D. V. Kolmykov, Ultramicroscopy **114**, 31 (2012).
[5] J. Barthel and A. Thust, Phys. Rev. Lett. **101**, 200801 (2008).
[6] B. Freitag, S. Kujawa, P. M. Mul, J. Ringnalda, and P. C. Tiemeijer, Ultramicroscopy **102**, 209 (2005).
[7] M. Linck, P. Hartel, S. Uhlemann, F. Kahl, H. Müller, J. Zach, M. Haider, M. Niestadt, M. Bischoff, J. Biskupek, Z. Lee, T. Lehnert, F. Börrnert, H. Rose, and U. Kaiser, Phys. Rev. Lett. **117**, 076101 (2016).
[8] S. Uhlemann, H. Müller, P. Hartel, J. Zach, and M. Haider, Phys. Rev. Lett. **111**, 046101 (2013).
[9] F. Börrnert, J. Renner, and U. Kaiser, Microsc. Microanal. **24**, 249 (2018).
[10] M. Lentzen, B. Jahnen, C. L. Jia, A. Thust, K. Tillmann, and K. Urban, Ultramicroscopy **92**, 233 (2002).
[11] K. Ishizuka, Ultramicroscopy **5**, 55 (1980).
[12] M. Haider, P. Hartel, H. Müller, S. Uhlemann, and J. Zach, Microsc. Microanal. **16**, 393 (2010).
[13] A. A. El-Barbary, R. H. Telling, C. P. Ewels, M. I. Heggie, and P. R. Briddon, Phys. Rev. B **68**, 144107 (2003).
[14] S. Uhlemann (private communication).
[15] S. Morishita, M. Mukai, K. Suenaga, and H. Sawada, Appl. Phys. Lett. **108**, 013107 (2016).
[16] H. Lichte, Ultramicroscopy **38**, 13 (1991).
[17] R. Erni, *Aberration-Corrected Imaging in Transmission Electron Microscopy* (Imperial College Press, London, 2010).
[18] F. Kahl, M. Linck, P. Hartel, H. Müller, S. Uhlemann, M. Haider, and J. Zach, in *The 16th European Microscopy Congress* (John Wiley & Sons, Chichester, 2017), p. 5742.